New analysis method for CCD X-ray data

T. Ishiwatari[a], G. Beer[b], A.M. Bragadireanu[c,d], M. Cargnelli[a], C. Curceanu (Petrascu)[c,d], J.-P. Egger[e], H. Fuhrmann[a], C. Guaraldo[c,*], M. Iliescu[c,d], K. Itahashi[f], M. Iwasaki[f], P. Kienle[a], B. Lauss[g], V. Lucherini[c], L. Ludhova[h], J. Marton[a], F. Mulhauser[h], T. Ponta[d], L.A. Schaller[h], D.L. Sirghi[c,d], F. Sirghi[c], P. Strasser[f], J. Zmeskal[a]

[a]*Stefan Meyer Institut für subatomare Physik, Boltzmanngasse 3, A-1090 Vienna, Austria*
[b]*Department of Physics and Astronomy, University of Victoria, P. O. Box 3055 Victoria B. C. V8W 3P6, Canada*
[c]*INFN, Laboratori Nazionali di Frascati, C. P. 13, Via E. Fermi 40, I-00044 Frascati, Italy*
[d]*Institute of Physics and Nuclear Engineering Horia Hulubei, IFIN-HH, Particle Physics Department, P.O. Box MG-6, R-76900 Magurele, Bucharest, Romania*
[e]*Institute de Physique, Université de Neuchâtel,1 rue A.-L. Breguet, CH-2000 Neuchâtel, Switzerland*
[f]*RIKEN Wako Institute, RIKEN (The Institute of Physical and Chemical Research), Wako-shi, Saitama, 351-0198, Japan*
[g]*Department of Physics, LeConte Hall 366, University of California, Berkeley, CA 94720, USA*
[h]*Physics Department, University of Fribourg, CH-1700 Fribourg, Switzerland*

Received 19 October 2005; accepted 27 October 2005
Available online 18 November 2005

Abstract

The analysis method developed for kaonic nitrogen X-ray data obtained at the DAΦNE electron–positron collider of Frascati National Laboratories using Charge-Coupled Devices (CCDs) in the DEAR experimental setup is described. Background events could be highly rejected by this analysis procedure. Three sequential X-ray lines from kaonic nitrogen transitions, showing good energy resolution, could be clearly identified, and the yields measured for the first time.

PACS: 36.10.Gv; 14.40.Aq; 29.30.Kv

Keywords: Pixel detectors; CCD data analysis procedure; Kaonic nitrogen energy spectra

1. Introduction

The DEAR (DAΦNE Exotic Atom Research) experiment at the DAΦNE ϕ-factory of Frascati National Laboratories is based on the detection of kaonic atom X-rays. Low absolute line yields and high background radiation in the electron–positron collider environment pose a serious experimental challenge. A new analysis method had to be developed for extracting accurate X-ray information from the CCD detectors, because the previously employed analysis techniques [1,2] were not sophisticated enough to be successfully employed for the DEAR data evaluation.

The main goal of the DEAR scientific program is to determine isospin-dependent $\overline{K}N$ scattering lengths by measuring the shift and the width, due to the strong interaction, of the $1s$ state in kaonic hydrogen and kaonic deuterium [3].

In the first stage of the DEAR program, the measurement of kaonic nitrogen was performed [4] with the aim to study machine background and setup performance, since the yields of kaonic nitrogen transitions are much higher than those of kaonic hydrogen. The possibility of precisely determining the charged kaon mass by studying the kaonic nitrogen atom was also explored in the preliminary measurement [5]. Three sequential X-ray lines of the kaonic nitrogen spectrum at 4.6, 7.6, and 14.0 keV

*Corresponding author. Tel.: +39 06 9403 2318; fax: +39 06 9403 2559.
E-mail address: carlo.guaraldo@lnf.infn.it (C. Guaraldo).

(corresponding to the $7 \to 6$, $6 \to 5$, and $5 \to 4$ transitions) were clearly identified and their yields measured for the first time [4].

In this paper, we give a detailed description of the analysis method applied to the CCD X-ray data. Section 2 describes the CCD analysis procedure, recalling briefly the characteristics of this detector and the features of X-ray events. In Section 3, the energy spectra obtained from the analysis are shown. In Section 4, the technique to determine the kaonic nitrogen transition yields is described. Conclusions are drawn in Section 5.

2. CCD analysis procedure

2.1. CCD X-ray detectors

The DEAR experimental setup is described in Ref. [4]. Charge-Coupled Devices (CCDs), which are sensitive to low-energy (below 20 keV) X-rays, were used as detectors. CCDs have a large number (1152×1242) of small-size pixels ($22.5 \times 22.5\,\mu m^2$). CCDs have unique capabilities of background rejection, high energy resolution, good detection efficiency, and intrinsic position resolution.

Identification of X-ray events and determination of their energies are achieved by taking advantage of the specific CCD features [1]. On one hand, photoelectrons produced by a low-energy X-ray are completely confined within the depletion layer in a few pixels (usually $\leqslant 2$). Thus their full energy can be measured. On the other hand, minimum ionizing particles (MIPs), which are the largest background for DEAR, and X-rays above 20 keV penetrate the depletion layer and create electron-hole pairs in the field-free region, where they spread over many pixels. Thus, only the energy deposit in or near the depletion layer, a fraction of the total energy, can be collected and read out.

A CCD image with events attributed to X-rays and background events from MIPs or γ-rays is shown in Fig. 1. Clusters consisting of one or two pixels are recognized as X-ray events, those with more hit pixels constitute the background. X-ray energy spectra are constructed via selection using this X-ray definition which will be corroborated in Chapter 3.1.

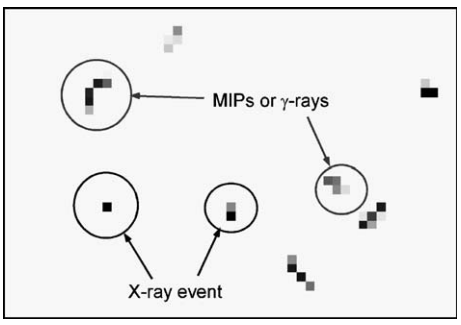

Fig. 1. CCD image. The grey scale is proportional to energy. MIPs or γ-rays create large-size events. Low-energy X-rays mainly create small-size events (one or two pixel hits).

2.2. Event definition via noise threshold determination

Even if a pixel was not hit during the exposure time, a charge content due to dark current from CCD readout is stored in such pixels. It can be seen as a Gaussian noise peak in the very-low-energy region of the energy spectrum. The peak location defines the offset, which is subtracted from each energy spectrum.

An event is then defined on the basis of the hit pixels whose signal is larger than a noise threshold, the remaining pixels being noise pixels. A cluster of hit pixels surrounded by only noise pixels is counted as one event, the energy of which is the sum of the hit pixels energies and whose size is defined by the number of hit pixels. Single-pixel events are size 1 events, double-pixel events are size 2 events, etc. In Fig. 2, several types of events are shown. For size $\geqslant 2$ events, events with energy higher than the upper limit of the ADC channels (4096 in a 12-bit ADC) are possible as the pixel contents get summed up.

The determination of the noise threshold is an essential requirement in the analysis procedure, since it determines event size, hence X-ray detection efficiency, energy resolution, and capability of background rejection. Several methods of noise threshold determination have been reported: see Refs. [2,6].

If an X-ray creates a double-pixel event, in which one of the two pixels has a larger fraction of signal and the other is registered as a noise pixel, this double-pixel event is wrongly selected as a single-pixel event, thereby resulting in a low-energy tail on an X-ray peak.

To minimize such misidentification of the event size, the noise threshold must be set to a small value, close to the readout noise fluctuations. If, however, this value is too small, a noise pixel might be selected as a hit pixel. Assuming that noise in the eight noise pixels surrounding a single-pixel event has a Gaussian distribution with mean value equal to 0 and standard deviation σ, the chance for this event to be selected as a single-pixel event is given by

$$p(E_{\mathrm{th}}) = \left(\frac{1}{\sqrt{2\pi}\sigma} \int_{-\infty}^{E_{\mathrm{th}}} \mathrm{e}^{-E^2/2\sigma^2}\, \mathrm{d}E \right)^8 \tag{1}$$

where E_{th} is a threshold value. Fig. 3 shows $p(E_{\mathrm{th}})$ plotted as a function of E_{th}/σ. When E_{th}/σ is over 3, the

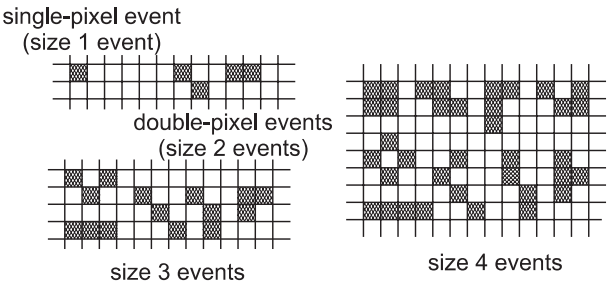

Fig. 2. Definition of events. One event is defined as a group (cluster) of connected hit pixels that are surrounded only by noise pixels. Events are named according to the number of pixels in a cluster.

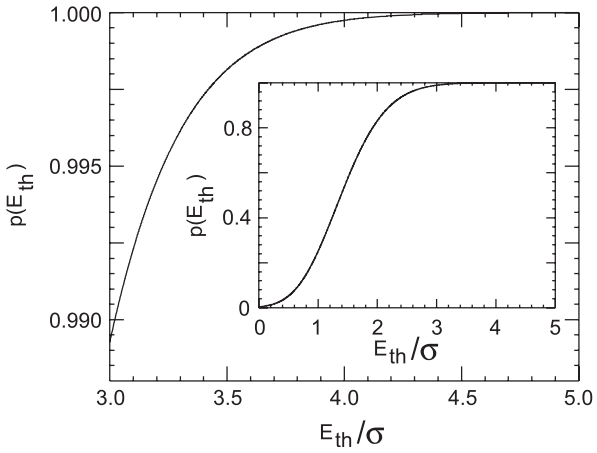

Fig. 3. Probability for noise pixels not to be selected as hit pixels as a function of the threshold. The horizontal axis gives the noise threshold in units of standard deviation. The noise peak is assumed to be a Gaussian function with standard deviation σ.

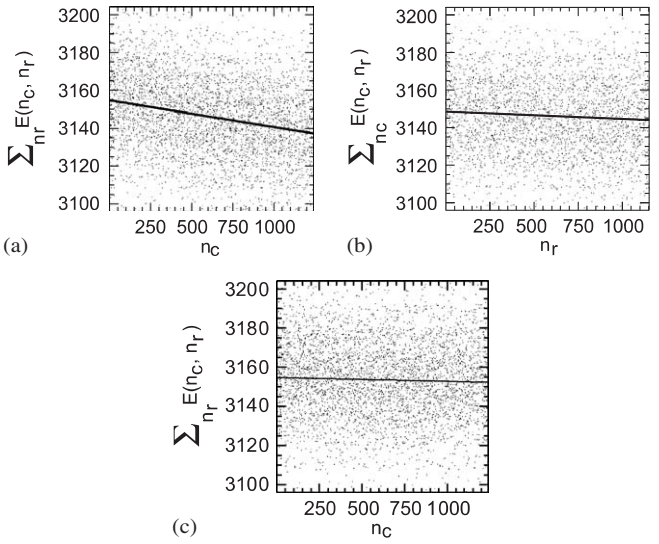

Fig. 4. Signal loss during transfer: (a) column transfer and (b) row transfer before the charge-transfer correction; (c) column transfer after the charge-transfer correction. $E(n_c, n_r)$ is the signal in the pixel of column n_c and row n_r.

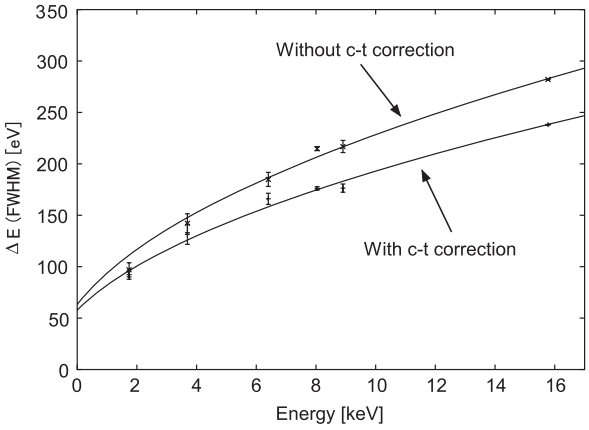

Fig. 5. X-ray energy resolution as a function of energy. Function (2) was used for the fit. After applying the charge-transfer (c–t) correction, the energy resolution is improved by about 10%.

probability for the single-pixel event to be misidentified as a double-pixel event is below 1%.

Threshold is determined run by run from the noise peak width, and is set at $E_{\rm th}/\sigma = 3-4$. Contribution of the low-energy tail on an X-ray peak is found to be only 0.4%. Thus, the effect of the low-energy tail is negligible.

2.3. Corrections for charge-transfer loss and energy resolution

Signals (charges) stored in a pixel are read out pixel by pixel when they are successively transferred out of the CCD. There is a small charge loss during the transfer. To study the dependence of a line position on the signal loss, the Zr Kα line from a Zr foil irradiated by an X-ray tube was fitted with a linear function. In the column transfer, signals decrease as the column number increases, as shown in Fig. 4(a), whereas the row transfer shows much less charge loss, as shown in Fig. 4(b). After the correction for charge-transfer loss in the column transfer, there is no significant dependence on the column number, as shown in Fig. 4(c).

In a CCD, the energy resolution ΔE (FWHM), plotted as a function of energy E in Fig. 5, can be fitted with the function:

$$\Delta E(\mathrm{FWHM}) = \sqrt{a^2 + bE} \qquad (2)$$

where a and b are parameters. The average energy resolution, after applying the linear charge-transfer correction, shows a 10% improvement.

2.4. Defect pixel rejection

Those pixels that have signals uncorrelated to incident particles are called "defect pixels". They are created during the chip fabrication or from radiation damage. Defect pixels with energy above ~1 keV (ADC channel 200) and a high hit rate are rejected because they may create artificial X-ray peaks.

The position distribution of hit pixels is expected to be uniform, thus the defect pixels may be selected by position analysis of each hit pixel. If a specific pixel shows a high hit rate, it is defined as a defect pixel.

Fig. 6 shows the hit rate of single-pixel events. Almost all the pixels have less than 4 hits, thus those pixels with at least 10 hits are defined as defect pixels.

To check whether the defect pixels are properly rejected, projections of the hit-pixel positions on columns/rows are plotted in Fig. 7, before and after defect-pixel removal. Spikes caused by events from defect pixels can be completely removed. Typically, a fraction of less than 10^{-6} pixels were selected as defect pixels.

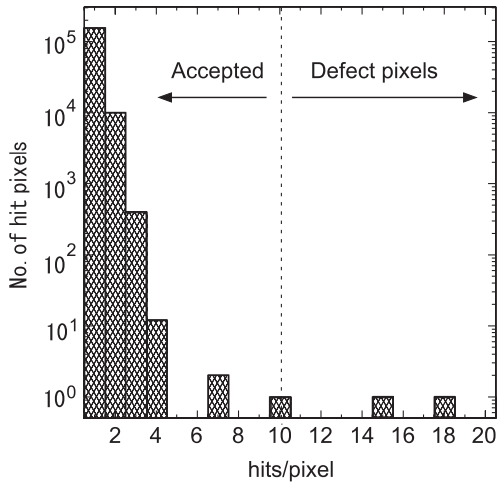

Fig. 6. Number of hit pixels selected as single-pixel events as a function of the number of hits/pixel in 3850 runs. Pixels in which over 10 hits occurred are removed as defect pixels.

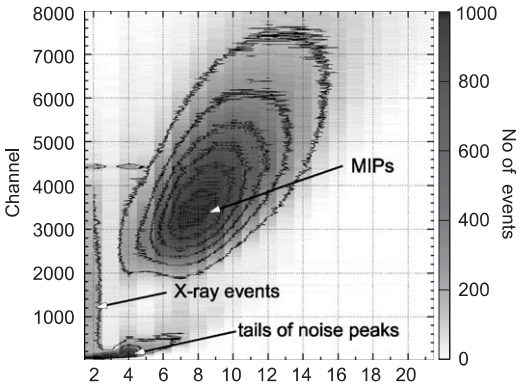

Fig. 8. The relationship between event size and deposited energy. The horizontal axis gives the event size and the vertical axis the ADC channel (energy deposit). The vertical axis is plotted up to twice the upper limit of ADC channels (up to about 35 keV). The gray scale gives the number of events. The central blob is due to minimum ionizing particles which penetrate the depletion layer. X-rays mainly create size $\leqslant 2$ events. The majority of the MIPs are well separated from X-ray events.

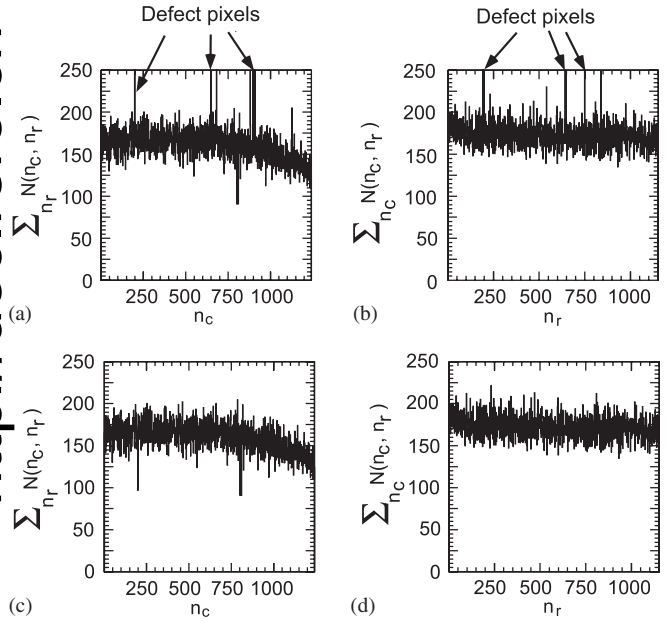

Fig. 7. Defect pixels are included in the distributions of counts of Figs. (a), (b). The vertical axis gives the number of counts in one column/row $\Sigma_{n_r/n_c} N(n_c, n_r)$. Events due to defect pixels are seen as spikes. Removing the defect pixels also removes spikes, see Figs. (c), (d).

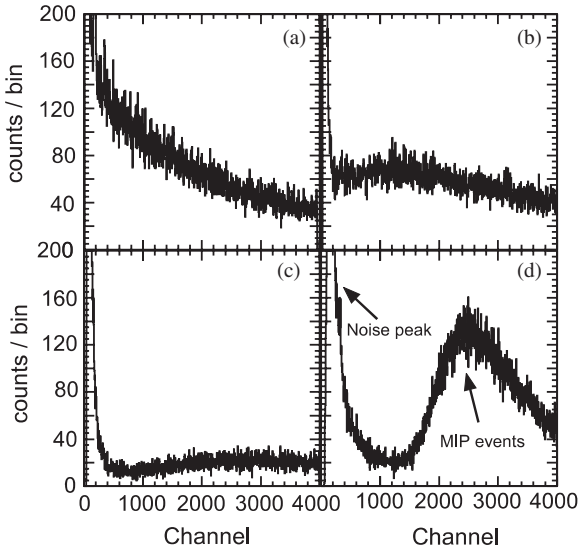

Fig. 9. X-ray spectra: (a) single-pixel events, (b) double-pixel events, (c) size 3 events, (d) size 4 events. The bumps seen in the spectra of size $\geqslant 2$ events are due to MIPs.

3. Results of the CCD analysis

3.1. Background rejection capability by cluster analysis

By applying the procedure described in Section 2, energy spectra of cluster events were produced. To show how events due to MIPs are rejected, the relationship between event size and energy deposit is plotted in Fig. 8.

A large concentration of events which appears as a blob at the center of the figure is due to MIPs penetrating the CCD depletion layer. The MIPs may be electrons or positrons lost from the beams and as well originating from the electromagnetic cascade initiated in the setup materials. The events due to X-rays are mainly size $\leqslant 2$ events. The majority of the MIPs are well separated from X-rays.

X-ray spectra (counts vs. channels) of size 1–4 events are plotted in Fig. 9. The background shape for single-pixel events is exponential, while that for size $\geqslant 2$ events has a bump created by MIPs. MIPs create preferentially size $\geqslant 4$ events, as seen in Fig. 8 and indicated by the large peak in Fig. 9(d). When only single-pixel events are considered, for instance as in Ref. [2], a better background rejection is expected. Since the probability of double-pixel events is high (about 40%), these events were also analyzed.

3.2. X-ray spectra of single- and double-pixel events

The ADC gains were adjusted to place the Zr Kα line at the same channel in the spectrum of each CCD. The spectra of single- and double-pixel events are plotted in Figs. 10 and 11. The kaonic nitrogen transitions are clearly seen. The signal/background ratio for the $6 \rightarrow 5$ peak is almost the same in both spectra. As well, the widths of the Zr Kα peaks are consistent in both spectra. Consequently, spectra of single- and double-pixel events can be added.

The spectrum of double-pixel events, extended up to twice the upper limit of ADC channels, is plotted in Fig. 12. The region from channels 3600 to 4000 contains ADC overflows which occurred in some CCDs, where the overflow started at a lower channel. Ag K peaks, coming from the adhesive material used to bond the CCD chips [7], are seen in channels 4400 and 5000. These Ag peaks were used as calibration lines for the upper part of the energy scale.

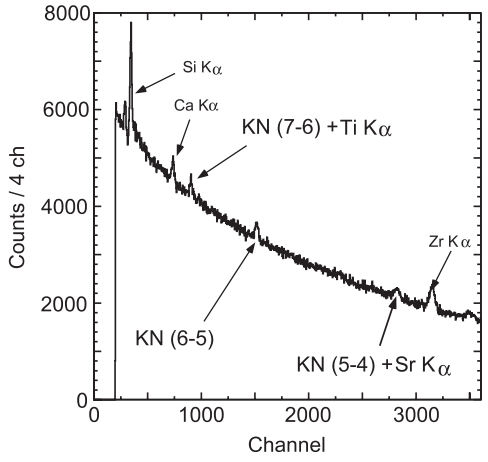

Fig. 10. X-ray spectrum obtained with only single-pixel events (events below ADC channel 200 were not plotted). The kaonic nitrogen transitions are clearly visible. X-ray lines from setup materials are also indicated.

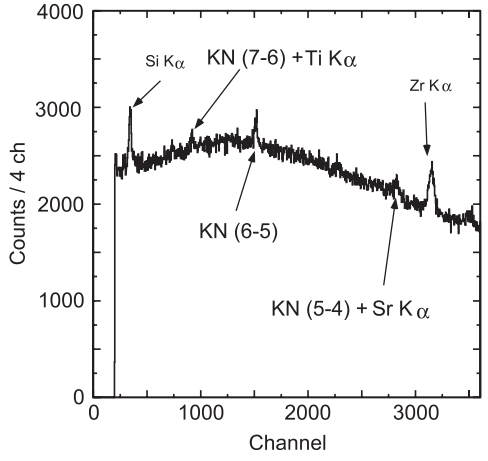

Fig. 11. X-ray spectrum obtained with only double-pixel events (events below ADC channel 200 were not plotted). The kaonic nitrogen transitions are clearly visible. X-ray lines from setup materials are also indicated.

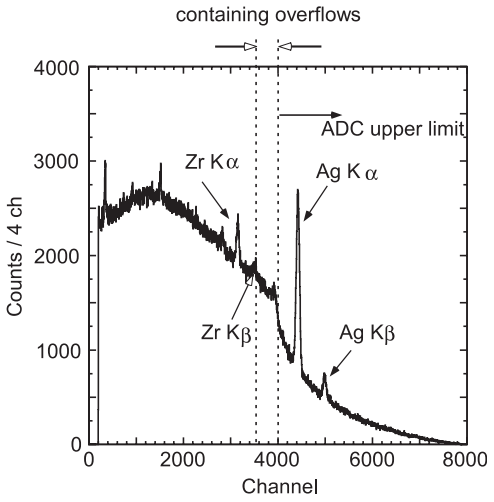

Fig. 12. X-ray spectrum of double-pixel events extended up to twice the upper limit of ADC channels. The region from channels 3600 to 4000 contains ADC overflows. There are prominent peaks in channels 4400 and 5000, which can be attributed to Ag K lines.

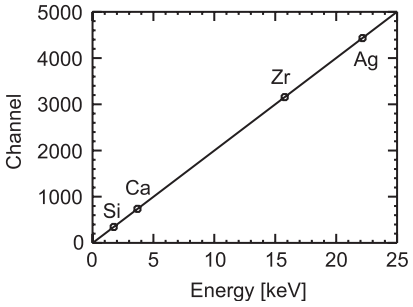

Fig. 13. The relationship between channel and energy. The fit errors are too small to be shown.

3.3. Energy calibration

To make the conversion from channel to energy, the known energies of Kα lines in Si, Ca, Zr, and Ag, taken from Ref. [8], were used. The Zr and Ag peaks were fitted with two Gaussians representing the $K\alpha_1$ and $K\alpha_2$ lines, since these lines can be disentangled. The observed linear energy dependence, plotted in Fig. 13, results in an energy calibration of better than 1 eV accuracy.

3.4. X-ray energy spectra

Fig. 14 shows the energy spectrum obtained by adding single- and double-pixel events.There are three sequential X-ray lines corresponding to transitions between levels of kaonic nitrogen. The kaonic nitrogen peak at 7.6 keV, corresponding to the $6 \rightarrow 5$ transition, is observed clearly. There are two other kaonic nitrogen peaks at 4.6 keV, corresponding to the $7 \rightarrow 6$ transition and 14.0 keV,

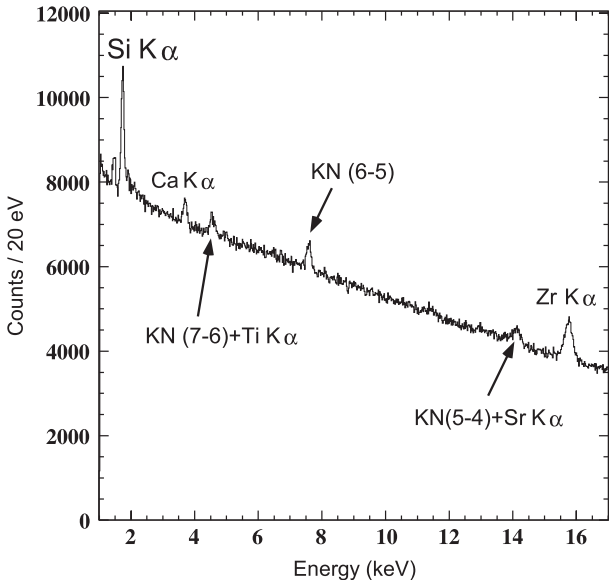

Fig. 14. X-ray energy spectrum with single- and double-pixel events added up.

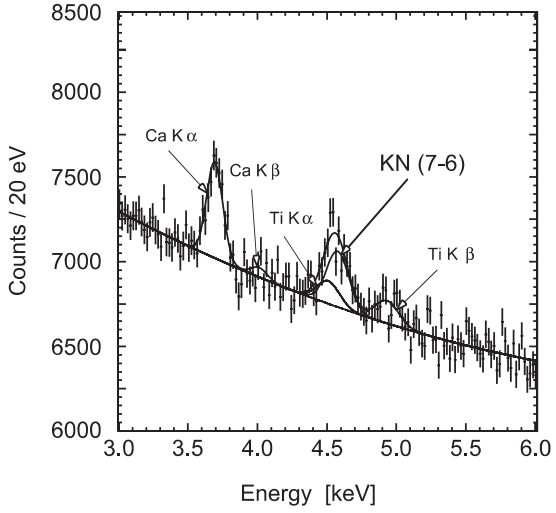

Fig. 15. Fit of the $7 \rightarrow 6$ transition peak. The kaonic nitrogen peak and the Ti Kα and Ti Kβ peaks are clearly separated by the fit. The relative intensities of the Ti Kα and Ti Kβ peaks and of the Ca Kα and Ca Kβ peaks were left as free parameters in the fit.

corresponding to the $5 \rightarrow 4$ transition, which partially overlap the Ti Kα and Sr Kα peaks, respectively.

As an example of the fit, the energy spectrum of the region from 3.0 to 6.0 keV is plotted in Fig. 15. The spectrum was fitted with 5 Gaussians for the Ca Kα, Ca Kβ, Ti Kα, Ti Kβ lines, and the kaonic nitrogen $7 \rightarrow 6$ transition. The fit was performed leaving the relative intensities of the Kα and Kβ peaks as free parameters, because in this low-energy region the X-ray attenuation in nitrogen gas and target window has a strong energy dependence. The background was fitted with a quadratic function. The measured numbers M_X of kaonic nitrogen X-ray events for each transition are given in Table 1.

Table 1
Measured number M_X of kaonic nitrogen X-ray events for each transition and corresponding signal/background ratio (S/B)

Transition	M_X ($\times 10^3$)	S/B ratio
$7 \rightarrow 6$	3.31 ± 0.69	1/15
$6 \rightarrow 5$	5.28 ± 0.38	1/10
$5 \rightarrow 4$	1.21 ± 0.32	1/37

4. Determination of X-ray yields

The global efficiency ε_X of having a kaonic nitrogen X-ray in a CCD is given by the kaon stopping efficiency in the target gas and the solid angle seen by the CCDs, assuming a 100% yield for the kaonic nitrogen transitions. The global efficiency ε_X at the energies of the kaonic nitrogen transitions was simulated using GEANT codes [9] and a code based on Ref. [10]. The X-ray attenuation in the nitrogen gas and the target window, as well as the thickness of the CCD depletion layer (intrinsic efficiency) were taken into account and put in the simulation. The results of the simulation are given in Table 2. Changing the ϕ-momentum in the simulation and making a comparison with experimental data taken with several degrader configurations, a 10% error was evaluated for the results of the simulation.

In this analysis method, only single- and double-pixel events were considered. However, X-rays can create size $\geqslant$ 3 events with a non-negligible probability. The probability R_X to form single- or double-pixel events can be written as

$$R_X = \frac{N_{S+D}}{N_{All}} \tag{3}$$

where N_{S+D} is the number of X-rays which form single- or double-pixel events, and N_{All} is the number of X-rays in all-size events. The values of R_X were measured with an X-ray tube at the energies of the kaonic nitrogen transitions, and are reported in Table 2.

CCD data contain events from both X-rays and MIPs. X-ray events cannot be detected if a pixel was already hit by a MIP. The number of X-ray events which can be detected can be simply evaluated from the number of non-hit pixels. During data taking, $(2.7 \pm 0.9)\%$ of all pixels were recorded as hit pixels, and thus the fraction of X-rays which can be detected is given by

$$\begin{aligned} R_{detect} &= 1 - (2.7 \pm 0.9) \times 10^{-2} \\ &= (9.73 \pm 0.09) \times 10^{-1}. \end{aligned} \tag{4}$$

This is the correction factor for multi-hit pixels due to MIPs.

The DEAR kaon monitor [11] counts the number of charged kaons N_{K^-} produced at the DEAR interaction point, with an uncertainty of about 3%. The *estimated number* of kaonic nitrogen X-ray events N_X (assuming a

Table 2
Global efficiency ε_X for detecting a kaonic nitrogen X-ray and probability R_X to form single- or double-pixel events

Energy	ε_X ($\times 10^{-4}$)	R_X
4.6	5.54	0.95
7.6	7.29	0.87
14.0	1.99	0.70

Table 3
Numbers of kaonic nitrogen X-rays N_X obtained by the simulation (assuming a 100% yield) and experimentally determined yields Y with their statistical (stat.) and systematic (syst.) errors [4]

Transition	N_X ($\times 10^3$)	Y ($\times 10^{-2}$)
$7 \to 6$	7.97 ± 0.79	41.5 ± 8.7 (stat.) ± 4.1 (syst.)
$6 \to 5$	9.59 ± 0.96	55.0 ± 3.9 (stat.) ± 5.5 (syst.)
$5 \to 4$	2.10 ± 0.21	57.4 ± 15.2 (stat.) ± 5.7 (syst.)

100% yield for each transition) can be written as:

$$N_X = N_{K^-} \varepsilon_X R_X R_{detect}. \quad (5)$$

For each transition, the N_X values are calculated using (5), where $N_{K^-} = 1.555 \times 10^7$ charged kaons, registered in $10.8\,pb^{-1}$ of integrated luminosity used for the analysis, ε_X and R_X are reported in Table 2, and R_{detect} is given by (4). The results are reported in Table 3.

The yields Y of each transition are then defined as the ratio M_X/N_X, where M_X is the *measured number* of kaonic nitrogen X-rays for each transition reported in Table 1. The yields of the three kaonic nitrogen X-ray transitions are reported in Table 3. The systematic error on the yields is due to the 10% error taken into account in the Monte Carlo simulation.

5. Conclusions

The CCD analysis method applied to the kaonic nitrogen X-ray data taken by the DEAR experiment at the DAΦNE collider, was described. Single- and double-pixel events were selected, and used for the analysis. The analysis procedure clearly identified a pattern of three X-ray lines from kaonic nitrogen transitions. The corresponding yields could be measured for the first time.

Acknowledgements

The DEAR collaboration acknowledges the DAΦNE machine crew for their excellent cooperation. Part of the work was supported by the European Commission within FP5, Transnational Access to Research Infrastructures, contract number HPRI-CT 1999-00088.

References

[1] J.-P. Egger, D. Chatellard, E. Jeannet, Part. World 3 (1993) 139.
[2] D. Sigg, Nucl. Instr. and Meth. A 345 (1994) 107.
[3] S. Bianco, et al., Riv. Nuovo Cimento 22 (1999) 1.
[4] T. Ishiwatari, et al., Phys. Lett. B 593 (2004) 48;
T. Ishiwatari, Ph.D. Thesis, Tokyo Institute of Technology, 2004.
[5] G. Beer, et al., Phys. Lett. B 535 (2002) 52;
G. Fiorucci, et al., Nucl. Instr. and Meth. A 292 (1990) 141;
D. Varidel, et al., Nucl. Instr. and Meth. A 292 (1990) 147.
[6] K. Yoshita, et al., IEEE Trans. Nucl. Sci. NS-46 (1999) 100.
[7] P. Gardiner, EEV Tech. Ltd., Marconi Applied Tech. Ltd., 2002, private communication.
[8] A.C. Thompson, et al., X-ray data booklet, LBNL/PUB-490 Rev. 2, Lawrence Berkeley National Laboratory, 2001.
[9] CERN Program Library.
[10] B.L. Henke, et al., At. Data Nucl. Data Tables 54 (2) (1993) 181.
[11] V. Lucherini, et al., Nucl. Instr. and Meth. A 496 (2003) 315.